# State-of-the-Art X-Ray Diffraction Experiments on Changes in Stratum Corneum Structure by the Application of Cosmetic Ingredients

Ichiro Hatta\* D

Division of Research, Nagoya Industrial Science Research Institute, Aichi, Japan

In the human stratum corneum, there are a variety of structures that can be observed by X-ray diffraction measurements. Based on these results and those obtained from other complementary techniques, the mechanism of effect upon applying cosmetic ingredients and related substances can be analyzed at the molecular level. Water is a fundamental substance in the stratum corneum. From the X-ray diffraction measurements, it was revealed that normal water content distribution is an important concept to maintain healthy skin. In addition, time-resolved X-ray diffraction measurements showed that glycerol can maintain the normal water content distribution for extended periods of time. The time-resolved methods solved various problems in investigating the effects of cosmetic ingredients. It was demonstrated that sodium dodecyl sulfate disrupted the long-period lamellar structure, and based on this result, the disrupted long-period lamellar structure could be restored by applying a mixture containing acylceramide. In addition, it was observed that the structures formed by the intercellular lipids are characteristically modified according to the ethanol application process, and from analyzing the results, it was suggested that the intercellular lipid matrix is composed of a large amount of a disordered hydrocarbon-chain packing state and that only the disordered state is dissolved by ethanol. Then, it was pointed out that this disordered state, with an average molecular weight of approximately 500 Da, plays an important role in the penetration of cosmetic ingredients into the intercellular lipid matrix. Nanoparticles consisting of lipids suspended in aqueous solution have attracted attention, and the use of time-resolved methods suggests that there exists a mechanism by which nanoparticles are reorganized on the surface of the stratum corneum and effective molecules are released into the stratum corneum.

**Key words:** X-ray, skin, water, lipid, lamellar, long period, sodium dodecyl sulfate, ethanol, glycerol, disordered, hydrocarbon chain, 500 Da, nanoparticle, short period

Division of Research, Nagoya Industrial Science Research Institute, 1-13 Yotsuyadori, Chikusa-ku, Nagoya, Aichi 464-0819, Japan

DOI: 10.69336/acst.Inv-2025-02



© The Society of Cosmetic Chemists of Japan 2025

This article is licensed under a Creative Commons Attribution 4.0 International License.

<sup>\*</sup>Corresponding author: Ichiro Hatta (E-mail: ichirohatta@gmail.com)

# 1. Introduction

Stratum corneum (SC), the outermost layer of the skin, functions as a barrier to prevent penetration of various harmful substances from outside the skin and to prevent abnormal water loss from inside the skin. SC consists of stacked flattened dead skin cells, corneccytes, each of which is surrounded by intercellular lipids. This arrangement is expressed by a bricks-and-mortar model, in which the corneccytes are bricks and the intercellular lipid matrix is mortar. The intercellular lipid matrix plays an important role in the barrier function. It is quite important to maintain the SC in a healthy state, which is supported by an undamaged structure. The lipids are mainly composed of ceramides, free fatty acids, and cholesterol. These lipid classes are present roughly in an equimolar ratio. Among them, ceramides are composed of more than 12 subclasses, with the carbon number of the chain being distributed widely, and free fatty acids have mainly saturated chain lengths also with the carbon number of the chain being distributed widely (e.g., Ref. 1)). Nevertheless, in human SC, the intercellular lipids form neat structures such as the long-period lamellar structure (LLS), the shortperiod lamellar structure (SLS),<sup>2)</sup> hexagonal hydrocarbon-chain packing structure (HEX), and orthorhombic hydrocarbon-chain packing structure (ORTHO).<sup>2,3)</sup> The corneccytes contain soft keratin filaments that lie roughly parallel to the flat surface of the cornecyte.<sup>2-4)</sup> Each of the above structures must have its own unique characteristics that are relevant to the function of the skin. From this viewpoint, it is important to carry out structure-based studies to clarify whether their function is enhanced or otherwise affected under various conditions, such as the use of cosmetics or detergents. In these structural studies, X-ray diffraction (XRD) is one of the powerful tools that can provide molecular-level mechanisms from the structural changes caused by several perturbations. In addition to knowledge obtained by the XRD, to establish the efficacy of cosmetic ingredients, it is essential to perform other methods such as electron microscopy, electron diffraction, neutron diffraction, confocal Raman microscopy, Fourier transform infrared, solid-state nuclear magnetic resonance, electron spin resonance, and liquid chromatography-mass spectrometry. Until now, many structural studies using SC lipid models have been carried out to clarify the effects of various molecules. However, some structures in SC cannot be reproduced by these models; for instance, SLS with a water layer cannot be realized. Additionally, the use of animals in research is discouraged in the cosmetics field. Therefore, I focused on the function of human SC obtained from cosmetic surgery as much as possible. In this review, I first describe how XRD experiments can provide structural information related to the condition of water in SC. This is one of the main subjects associated with cosmetics. Second, I introduce a unique method for observing detailed structural changes upon applying cosmetic ingredients and related molecules to human SC. Third, I will discuss some results obtained using this method successfully.

# 2. What Structures Can Be Observed in SC Using XRD?

# 2.1. Typical XRD observed in human SC

In Figs. 1A–1C, a typical XRD intensity profile observed in human SC is shown. For details of the experiments, see Ref.  $^{5)}$  The scattering vector on the horizontal axis, q or S, is generally given as follows:

$$q = \left(\frac{4\pi}{\lambda}\right) \sin\left(\frac{2\theta}{2}\right) \text{ or } S = \left(\frac{2}{\lambda}\right) \sin\left(\frac{2\theta}{2}\right),$$
 (1)

where  $\lambda$  is the wavelength of an incident X-ray beam and  $2\theta$  is the scattering angle. The diffraction peaks appear according to the Bragg equation:

$$2d \sin\theta = n\lambda, \tag{2}$$

where d represents spacing due to periodic arrangement of electron density distribution such as lamellar and hydrocarbon-chain packing in SC and n is an integer. Therefore, the diffraction peaks occur at

$$q = \frac{2\pi n}{d} \text{ or } S = \frac{n}{d}.$$
 (3)

In SC, the molecular arrangements of lipids are schematically shown in Fig. 2A for the lamellar structures and in Fig. 2B for the hydrocarbon-chain packing structures. These structures have been observed not only in human SC but also in hairless mouse and other mammalian SCs. However, ORTHO was not observed in pig SC. Therefore, although only human SC is currently used in studies on cosmetic science, it is useful to refer to the results obtained from the measurements of hairless mouse SC, and so on. In human SC, the spacing of LLS has been reported to be 13.4 nm.<sup>2)</sup> Even in SC of the same species, this spacing is distributed around 13 nm; however, in each sample a definite repeat periodicity is

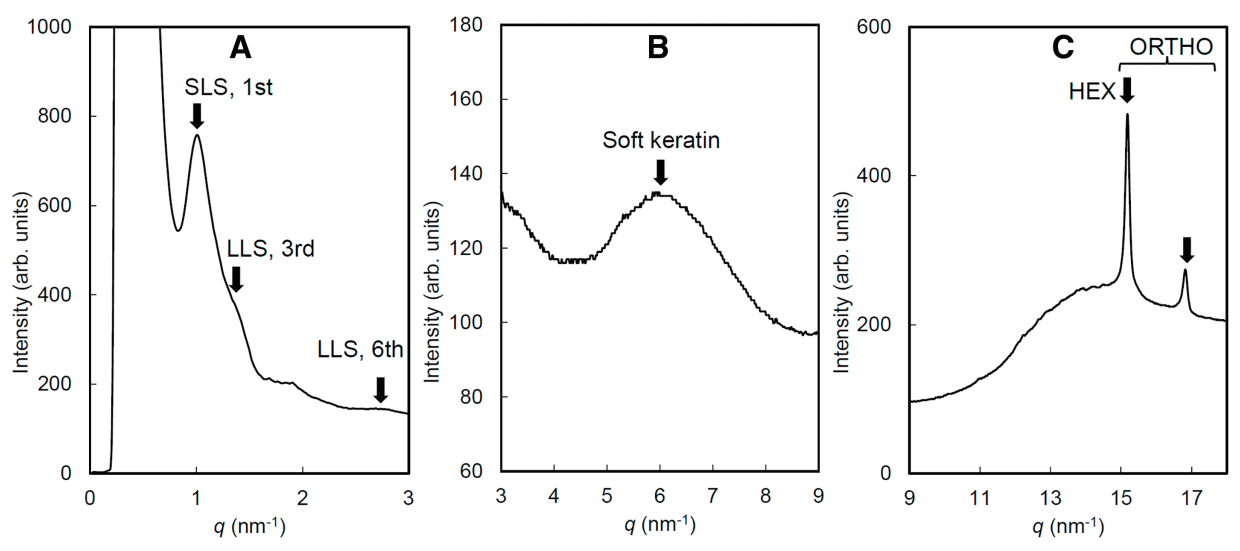


Fig. 1 A typical plot of X-ray diffraction intensity profile of human stratum corneum measured in the range of q = 0.2–  $18 \text{ nm}^{-1}$ . (A) Small-angle diffraction intensity profile. (B) Intensity profile for soft keratin around  $q = 6 \text{ nm}^{-1}$ . (C) Wide-angle diffraction intensity profile. In the profile below  $q = 0.2 \text{ nm}^{-1}$ , the intensity was blocked by a direct beam stop. arb. units, arbitrary units; LLS, long-period lamellar structure; HEX, hexagonal; ORTHO, orthorhombic; SLS, short-period lamellar structure

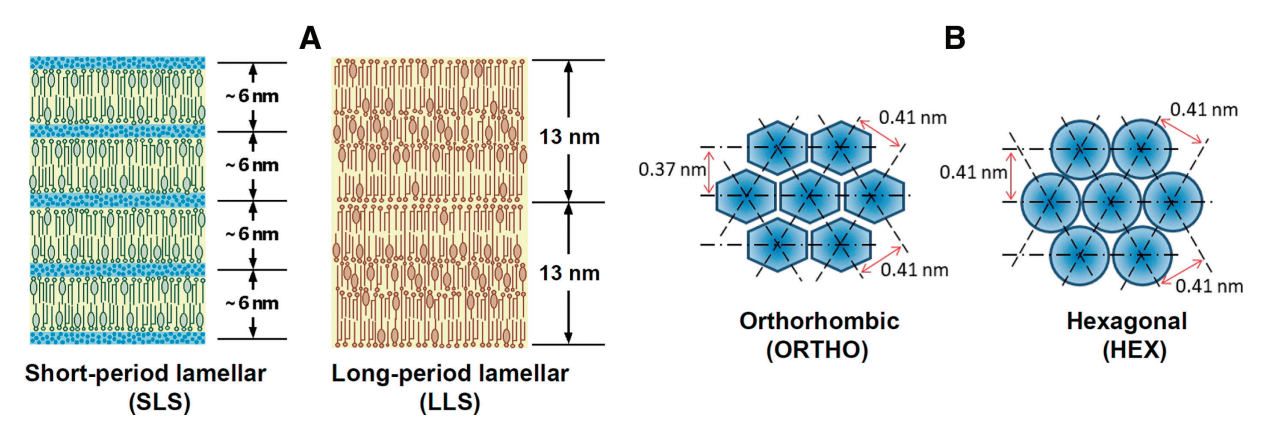


Fig. 2 (A) Schematic view of short-period lamellar structure and long-period lamellar structure, which are composed of ceramides, free fatty acids, cholesterol, and water (for the former). (B) Schematic view of orthorhombic and hexagonal hydrocarbon-chain packing structures.

observed. In mammalian SC, the spacing lies between 12.0 and 13.6 nm.<sup>6,7)</sup> SLS has a periodicity of about 6 nm, which depends on the water content in SC; that is, the spacing increases almost linearly with the water content.<sup>6,8)</sup> In connection with this result, neutron diffraction analysis of human SC has shown that this spacing increases upon hydration from a dry state.<sup>9)</sup> For ORTHO, sharp diffraction peaks due to the spacings of 0.41 and 0.37 nm are observed.

It should be noted that the above results are complementary to those of electron microscopy. It is not easy to derive the electron density distribution from the results of the XRD. However, by electron microscopy observation, the electron density distribution of LLS and SLS can be obtained for human SC. LLS in Fig. 2A is drawn based on a tri-lamellar structure (the so-called Landmann unit) observed by electron microscopy. <sup>10,11)</sup> For SLS in Fig. 2B, the bilayer structure with the short repeat distance was observed by cryo-electron microscopy. <sup>12)</sup>

As seen in Fig. 1A, the small-angle XRD peaks due to LLS and SLS appear in a human SC sample prepared by cutting from skin. As seen in this figure, in human SC, a strong first-order (n = 1) diffraction peak of SLS occurs at  $q = 1.00 \text{ nm}^{-1}$  (= $(2\pi \times 1/6.3) \text{ nm}^{-1}$ ) as the main peak, and the relatively weak third-order (n = 3) diffraction peak of LLS appears as a shoulder centered around  $q = 1.38 \text{ nm}^{-1}$  (=  $(2\pi \times 3/13.6) \text{ nm}^{-1}$ ), which is consistent with the results obtained by Bouwstra et al.<sup>2)</sup> and can be inferred from a small but clearly visible sixth-order peak ( $q = 2.76 \text{ nm}^{-1}$ ). Such a diffraction intensity profile is characteristic of the small-angle XRD intensity profile of human SC. Some human SC samples show



Fig. 3 (A) The corneccyte is plate-shaped and its surface shape is roughly hexagonal. (B) Within a "brick," the long axis of soft keratin filaments lies roughly parallel to the flat surface (x-y) plane) of the corneccyte.

a distinct third-order diffraction peak, as shown later. In Fig. 1B, a broad peak at  $q = 6.0 \text{ nm}^{-1}$  (corresponding spacing: 1.0 nm) due to soft keratin appears. This peak might be due to the distance between coiled-coil  $\alpha$ -helix chains of the soft keratin, which lies parallel to the flat surface of the corneocyte. As shown in Fig. 1C, in the wide-angle region, ORTHO peaks appear at q = 15.2 and  $16.8 \text{ nm}^{-1}$  (corresponding spacings: 0.41 and 0.37 nm, respectively).<sup>3)</sup> However, it is hard to detect a HEX peak for the lattice constant, 0.41 nm, by the XRD since it lies at the same position as one of the ORTHO peaks. According to White et al., it was pointed out that the XRD at 0.417 nm could partly be due to a hexagonal packing.<sup>13)</sup> Electron diffraction allows observation of a single domain of HEX using a narrow electron beam; therefore, the existence of HEX has been clearly demonstrated.<sup>14,15)</sup> As shown in Fig. 1C, behind the strong, sharp peaks at q = 15.2 and  $16.8 \text{ nm}^{-1}$ , a broad hump lies at  $q \approx 14 \text{ nm}^{-1}$  due to soft keratin. Recently, it has been revealed that SLS and ORTHO are in the same domain and are not independent structures.<sup>16-19)</sup>

# 2.2. Other X-ray scattering and diffraction intensity profiles of SC

The X-ray scattering and diffraction intensity profiles of SC reflect all the electron density distribution within SC. For instance, there are many factors that cause the X-ray scattering intensity to increase toward q = 0, as exemplified by the bricks-and-mortar model.<sup>20)</sup> For SC, in the low q region, the X-ray scattering curve that forms the background of the diffraction intensity profile is expressed by

$$I(q) \sim q^{-\beta}. \tag{4}$$

where the exponent  $\beta$  ranges from 2 to 4.<sup>21)</sup> In Fig. 1A, the regions q = 0.3-0.4 nm<sup>-1</sup> and  $q \ge 2.5$  nm<sup>-1</sup> can be expressed as the background given by Eq. (4). By subtracting this background, the diffraction peaks in the small-angle region can be derived. This subtraction procedure is robust, and small changes in the power function do not result in significant changes in the peak positions or intensities. In the analysis by Doucet et al., the  $\beta$  of the background was set to 3.<sup>4)</sup>

As seen in Fig. 1A, in the small-angle region, in addition to the above background, other backgrounds occur. To analyze the XRD peaks in this region, this background must also be subtracted. For instance, in the delipidated human SC, in addition to the above background, a broad peak appears between the first-order SLS peak and the third-order LLS peak, and therefore this contribution must be subtracted in the analysis of the XRD peaks. Furthermore, it should be noted that in human SC, the XRD intensity profile includes the contribution from the mixture of 1-, 2-, and 3-unit layers, where 1-unit layer is composed of the Landmann unit. Particularly in the small-angle region, 1-unit layer produces a broad peak between the first-order SLS peak and the third-order LLS peak. Therefore, it should be noted that the XRD intensity profile arises not only from multilamellar SLS and LLS but also from the sum of several unit layers.

In addition, it is worthwhile to note that for LLS of human SC, sharp diffraction peaks appear when an SC sample is heated up to 120°C and cooled down to room temperature.<sup>2)</sup> Therefore, this indicates that before heating, the human SC sample already contains intercellular lipids capable of forming LLS.

In the small-angle region, sometimes a small peak appears at  $q = 1.88 \text{ nm}^{-1}$  due to the formation of a cholesterol crystal with a lattice constant of 3.35 nm.

As shown in Figs. 3A and 3B, in corneccytes, soft keratin filaments run almost parallel to the plane surface.<sup>4)</sup> The spacing between coiled-coil  $\alpha$ -helix chains in the soft keratins gives rise to a very broad and weak peak around  $q = 6.0 \text{ nm}^{-1}$  (corresponding spacing: 1.0 nm), which remains after lipid extraction.

As seen in Fig. 1C, behind the sharp ORTHO peaks, a broad hump lies. Generally, the broad hump is mainly composed of a maximum around  $q = 14 \text{ nm}^{-1}$  (corresponding spacing: 0.45 nm), and in addition, depending on the water content in SC, a broad peak having a maximum near  $q = 19 \text{ nm}^{-1}$  (corresponding spacing: 0.33 nm) is superimposed. Furthermore, the broad hump around  $q = 14 \text{ nm}^{-1}$  is composed of 2 contributions. One is a broad peak due to soft keratin, and the other is a broad peak due to a disordered hydrocarbon-chain packing state (or fluid state [FLUID]). Since each

structure has a function, it is very important to separate these overlapping peaks and to discuss them independently. In particular, the latter structure plays an important role in the penetration of molecules into SC. It is sometimes argued that increasing the ratio of HEX to ORTHO, which occurs by raising the temperature or by treatment with a penetration enhancer, is effective in increasing the permeability of topical substances; however, first of all, the FLUID, which exists originally in SC, must be taken into consideration.

In addition to ORTHO mentioned above, several other minor orthorhombic hydrocarbon-chain packing structures exist. For instance, from the electron diffraction observation in human SC, an orthorhombic hydrocarbon-chain packing structure with the lattice constants of 0.42 and 0.39 nm was observed;<sup>15)</sup> by the wide-angle XRD measurement in hairless mouse SC, the splitting of the diffraction spots for the lattice constant 0.37 nm was observed.<sup>23)</sup>

# 3. Effect of Water on the Structure of SC

#### 3.1. Methods examining water in SC

Water is one of the key factors for maintaining healthy skin. There are many devices available that can evaluate the water condition of skin *in vivo*. The degree of water evaporation from the skin surface is associated with the barrier function and is assessed by measuring transepidermal water loss (TEWL) *in vivo*.<sup>24)</sup> TEWL is one of the most commonly used indicators of the skin barrier integrity and plays an important role in testing areas such as transdermal drug delivery, skin aesthetics, and topical cosmetic irritation. Meanwhile, high-frequency electrical conductance or capacitance measurement is an important *in vivo* method to evaluate the water content in SC.<sup>25)</sup> It is possible to evaluate water retention efficacy upon applying various cosmetic ingredients. In SC, water is mainly stored in corneocytes, and additionally a small amount of water is localized in SLS, which plays an important role in water regulation.

# 3.2. Changes in SLS and LLS by water

As mentioned above, in human SC the small-angle XRD intensity profiles relating to the structures of SLS and LLS are somewhat complicated. Whereas in hairless mouse SC, the sharp XRD peaks of SLS and LLS can be observed clearly. For hairless mouse SC, successive variation of the small-angle XRD intensity profile as a function of the water content was observed.<sup>6)</sup> Although this study was performed not on human SC but on animal SC, it was included here because it provides the clearest results on this issue to date. Later, it will be shown that consistent results were obtained in human SC. In Fig. 4A, the small-angle XRD intensity profile in the region S = 0-4 nm<sup>-1</sup> (or q = 0-2.5 nm<sup>-1</sup>) is shown for water content from 0 to 80 wt%. Throughout this paper, the water content is defined as

Water content (wt%) = 
$$\frac{\text{Weight of water}}{\text{Weight of (dry stratum corneum + water})} \times 100.$$
 (5)

Around  $S = 1.5 \text{ nm}^{-1}$ , the first-order XRD SLS peak and the second-order XRD LLS peak appear close to each other. The XRD intensity profile of this region was analyzed by fitting to an intensity profile consisting of 2 Lorentzian curves and a linear background. Here, Lorentzian curves were used in peak fitting because the peaks are very sharp. The spacings of LLS and SLS and the full width at half maximum were analyzed as a function of the water content, and they are shown in Figs. 4B and 4C, respectively. As seen in Fig. 4B, half of the spacing for LLS, about 6.75 nm (= 13.5/2 nm), is nearly constant with respect to the water content, whereas the spacing for SLS increases linearly with the water content. As seen in Fig. 4C, with increasing water content, the full widths at half maximum of LLS and SLS show similar changes; first decreasing, then reaching a minimum at a water content of around 25 wt%, and finally rising. The results on human SC obtained by Bouwstra et al.<sup>2)</sup> are consistent with the above results. Namely, in human SC, the small-angle XRD measurements were performed at water contents of 6, 20, 40, and 60 wt%. The peak intensity of LLS is maximum at a water content of 20 wt%. On either side of this water content, the peak intensity of LLS decreases significantly. Also, the spacing of LLS does not vary with the water content. By neutron diffraction,<sup>9)</sup> it has been observed that an increase in the spacing of SLS from 5.7 to 6.2nm appears by exposing a human SC sample to D<sub>2</sub>O vapor. This result is consistent with that obtained in hairless mouse SC as seen in Fig. 4B. Nakazawa et al.8) performed the small-angle XRD measurement on human SC as a function of the water content and found that the spacing of SLS increased with the water content, as well as a narrowing of the full width at half maximum at a water content between 20 and 30 wt%, almost agreeing with the results on hairless mouse SC. Thus, with regard to the behavior of SLS and LLS as a function of the water content, the results obtained in hairless mouse SC offer essential characteristics.

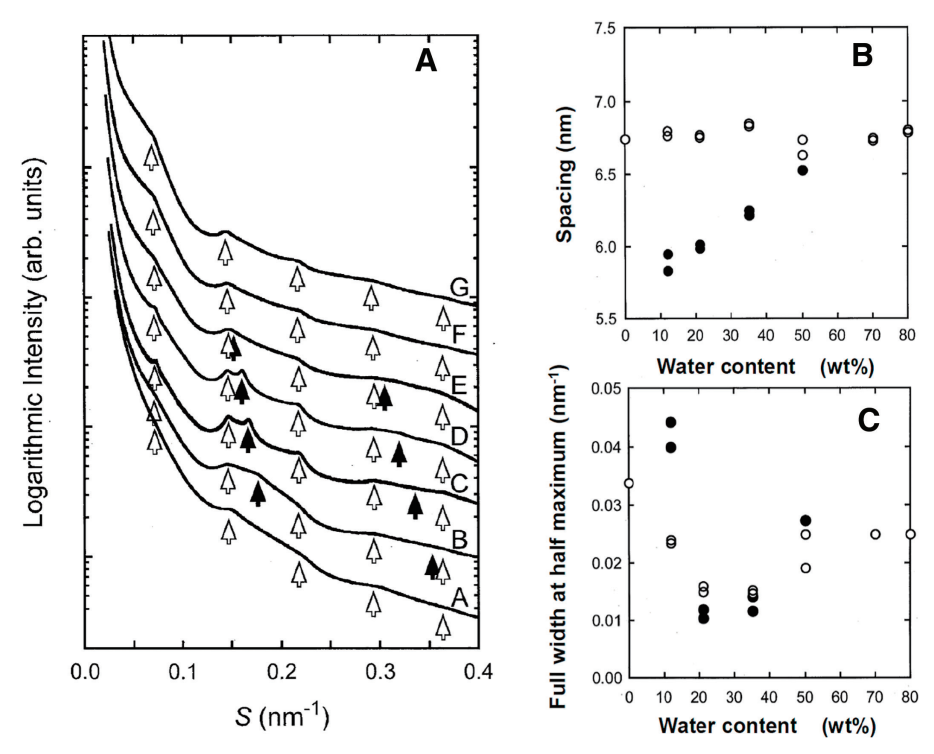


Fig. 4 (A) Small-angle X-ray diffraction intensity profile in hairless mouse stratum corneum as a function of the water content, where the vertical axis is shown on a logarithmic scale. The water contents are as follows: A, 0 wt%; B, 12 wt%; C, 21 wt%; D, 35 wt%; E, 50 wt%; F, 70 wt%; G, 80 wt%. The open arrows indicate the peak positions of the long-period lamellar structure, and the filled arrows indicate the peak positions of the short-period lamellar structure. (B) Dependence of the spacings on the water content for the second-order diffraction of the long-period lamellar structure (○) and for the first-order diffraction of the short-period lamellar structure (○). (C) Full widths at half maximum of X-ray diffraction peaks for the second-order X-ray diffraction of the long-period lamellar structure (○) and for the first-order X-ray diffraction of the short-period lamellar structure (○).

The result of the small-angle XRD measurements suggests that the increase in the spacing of SLS is caused by an increase in the thickness of the water layer formed between adjacent polar head groups in the lipid bilayer. The result that the full width at half maximum becomes narrow in SLS indicates that this structure is stabilized at a water content of 25 wt%. The full width at half maximum of LLS also narrows at a water content of 25 wt%, although the role is currently unclear. This behavior may be correlated with the phenomenon that, with increasing water content, the 2-fold spacing of SLS becomes close to the spacing of LLS and therefore this interaction may promote the stability of SLS. In addition, for the hydrocarbon-chain packing, the ORTHO structure is also stabilized at a water content of 25 wt%. <sup>18,19</sup> In connection with this fact, Toyoshima et al. <sup>19</sup> recently revealed a clear correlation between ORTHO and SLS.

#### 3.3. Changes of structures in soft keratin by water

Water in human SC is stored mainly in corneocytes, and soft keratin is present within the corneocytes and interacts with water. Broad XRD peaks associated with the soft keratin in human SC appear at q = 6.0 and  $14 \text{ nm}^{-1}$  (corresponding spacing: 1.0 and 0.45 nm, respectively). As shown in Fig. 1B, the former peak is independent from the other XRD peaks and is therefore relatively easy to analyze. The results are shown in Fig. 5A for the spacing and Fig. 5B for the full width at half maximum. From the spacing, we infer that this is due to the distance between the coiled-coil  $\alpha$ -helix chains of soft keratin. As seen in Fig. 5A, this spacing increases with the water content, and around a water content of 25 wt%, the rate of increase becomes weak. As shown in Fig. 5B, the full width at half maximum of the XRD peak increases with the water content and around a water content of 25 wt% becomes almost flat. These facts suggest that soft keratin filaments become flexible up to the water content of 25 wt%, and above 25 wt%, the interaction between water and soft keratin filaments becomes weak, resulting in weaker softening.

#### 3.4. Other comprehensive evidence for characteristic behavior at the water content of 25 wt%

Clear evidence indicating that 25 wt% is the key water content in skin has been obtained from differential scanning calorimetry (DSC). The transition enthalpy at 0°C has been measured as a function of the water content in human

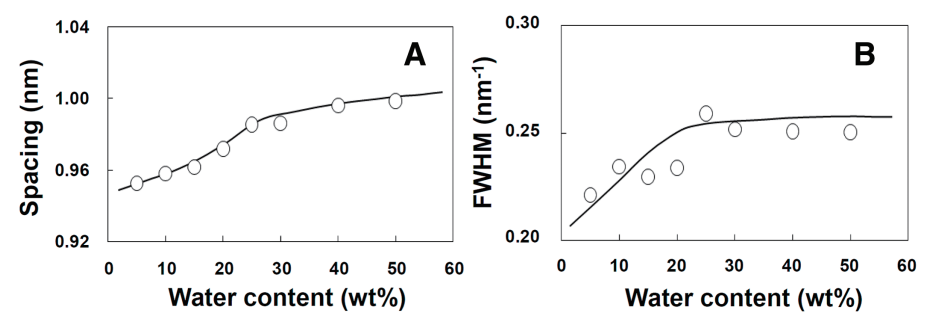


Fig. 5 (A) Change of spacing associated with the distance between the coiled-coil α-helical chains of soft keratin as a function of the water content. (B) Change of the FWHM of the X-ray diffraction for the coiled-coil α-helical chains of soft keratin as a function of the water content.<sup>8)</sup> FWHM, full width at half maximum

SC.<sup>26,27)</sup> Imokawa et al.<sup>27)</sup> observed that the transition enthalpy of water decreases as the water content is reduced and does not appear below the water content of 25 wt%, as defined in Eq. 5. This result indicates that if the water content is less than 25 wt%, there are water molecules tightly bound within the SC, while if the water content is greater than 25 wt%, the excess water molecules above 25 wt% become free.

Another important evidence was obtained from confocal Raman microscopy. This is a powerful method to observe the depth intensity profile of the water content in human SC *in vivo*.<sup>28)</sup> The water content of skin is 20–30 wt% near the skin surface and then rises in a sigmoidal-shaped manner to a water content of 60–70 wt% with a plateau.<sup>29,30)</sup> The water content at the skin surface is consistent with the value of 25 wt% revealed by the small-angle XRD and DSC. Therefore, it can be stated that water at approximately 25 wt% near the normal skin surface is retained as bound water. Furthermore, the increase in the water content in SC toward depth can be attributed to the increase of free water. Near the surface of SC, bound water forms around soft keratin in SC, and free water forms further deeper within corneocytes. Bouwstra et al.<sup>31)</sup> showed from cryo-scanning electron microscopy of human SC that the thickness of the corneocyte increases toward depth. This supports the increase in the water content observed by confocal Raman microscopy. Consistent with this fact, Egawa et al.<sup>32)</sup> observed by confocal Raman microscopy that the thickness of human SC increases after hydration. Furthermore, considering the normal water distribution in human SC, an important result obtained by confocal Raman microscopy is that the water content of human SC near the skin surface increases upon substantial external water application, but this water content subsequently returns to 25 wt% over time.<sup>33)</sup>

From the barrier function perspective, it is noteworthy that in healthy skin, water at the skin surface is maintained at 25 wt% as bound water and the structure of SLS is stabilized at a water content of 25 wt%, not in the intercellular lipid matrix but in SC, and both mechanisms are essential for healthy skin.<sup>19)</sup>

## 3.5. Relationship between structures in SC and electrical measurements and TEWL

Electrical measurements, such as capacitance and impedance measurements, have been widely used to assess the *in vivo* water content within human SC. As mentioned above, the water content is distributed within SC, so the values obtained by these electrical measurements are likely to represent some average water content in the skin. Furthermore, due to the high dielectric constant of water, electrical measurements could detect the contribution of water in the deeper SC. Meanwhile, TEWL may reflect the condition of the skin surface, since the final barrier to water evaporation is the surface. In connection with this fact, it is of interest to note that TEWL was increased in atopic skin, but TEWL does not seem to correlate with capacitance.<sup>34)</sup> According to Egawa et al.,<sup>35)</sup> when the skin is exposed to a low humidity environment, the skin surface roughness increases; as a result, TEWL also decreases. Thus, each of the commonly used methods, the electrical measurements and TEWL, for assessing skin hydration has its own place.

# 4. Minute Structure Changes in the SC after Application of Active Substances

# 4.1. Solution cell for the high-resolution detection of structure changes by XRD

As mentioned above, the lamellar and hydrocarbon chain packing structures are composed of a complex mixture of various intercellular lipids, so it is not easy to reproduce the structures. Therefore, it is essential to perform XRD experiments on *ex vivo* human SC. Moreover, the small-angle XRD intensity profile of human SC is not as simple as that of animal SCs. To perform XRD experiments on human SC, we have to solve these problems. Then, we developed the so-called "solution cell."<sup>36</sup>

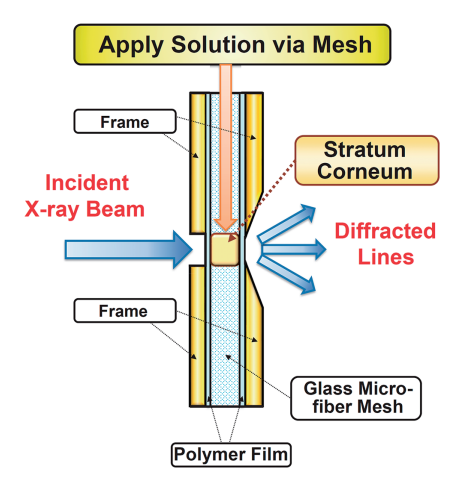


Fig. 6 A solution cell developed to detect minute structural changes in a single stratum corneum sample with high time resolution and high accuracy, when an aqueous solution containing cosmetic and pharmaceutical ingredients is applied to a stratum corneum sample.

The solution cell is schematically drawn in Fig. 6. A thin human SC sheet was crumpled and embedded in a central hollow surrounded by a fine mesh (grade: GMF 150, Whatman plc, Little Chalfont, UK), composed of a glass microfilter. This glass microfiber mesh was used to sustain the SC sample and allowed solution flow through the mesh without clogging. The front and rear surfaces of the cell were sealed by a pair of thin polymer films with a thickness of about  $10 \mu m$ . Thus, a fixed SC sample would be surrounded by a sufficient solution when the solution was applied via the mesh. The incident X-ray beam impinged on the front surface of the polymer film window. To detect the structural changes of human SC with high time resolution and high precision when applying solutions containing various substances, we performed the XRD measurements using synchrotron X-ray.

This method has the unique advantage of being able to measure the same location in a single sample during the measurement; that is, using the solution cell, an SC sample fixed with the mesh is immersed in solution, and then we are able to detect minute structural changes within seconds in a single SC sample. As a result, this method can overcome the problem of individual differences among SC samples. Normally, due to individual differences, the XRD peak intensity depends on the SC sample: in some SC samples, the peak intensity is large; in others, it is small. In all cases, however, when a solution is applied to an SC sample, the same systematic XRD intensity change can be observed. We then can detect the structural changes when a solution with cosmetic or drug is applied to a human SC sample.

## 4.2. Role of glycerol in maintaining normal water distribution in the SC

To show the usefulness of the solution cell, the effectiveness of glycerol in maintaining normal water conditions within human SC was investigated. Glycerol is classified as a humectant and is known to play an important role in moisturizing the skin. To elucidate this mechanism at the molecular level, XRD can be used to observe the structural changes in human SC upon application of an aqueous solution of glycerol. Yamada et al.  $^{17,18}$ ) studied this subject with a focus on 2 points: First, the XRD measurements were performed using the solution cell to detect the minute structural changes not only in intercellular lipids but also in soft keratin; second, they focused on observing the structural changes that occur during the drying process of human SC samples, aiming to address the problem that dry environments have severe effects on skin. In this experiment, a human SC sample was immersed in water or an aqueous solution of glycerol or diglycerol for 120 min, and then dried by flowing  $N_2$  gas for 40 min, during which the XRD intensity was measured every 30 s.

Figures 7A and 7B show the XRD intensity profiles near q = 6 nm<sup>-1</sup> during the drying of single SC samples treated with water and with an aqueous solution of 10% glycerol, respectively. This peak due to the coiled-coil  $\alpha$ -helix chains of soft keratin was analyzed by fitting to a Gaussian function with a straight background. The results for the spacing versus drying time are shown in Figs. 8A and 8B for the samples treated with water and with the aqueous solution of 10% glycerol, respectively. Although clear differences are not visible in the intensity profiles between Figs. 7A and 7B, the change in spacing as a function of drying time is clearly distinguishable, as seen in Figs. 8A and 8B: the water-treated sample has a steeper downward slope, whereas the 10% glycerol-treated sample has a more gradual downward slope. The slopes for water and aqueous solutions of 10% diglycerol, together with 10% diglycerol, are summarized in Table 1.

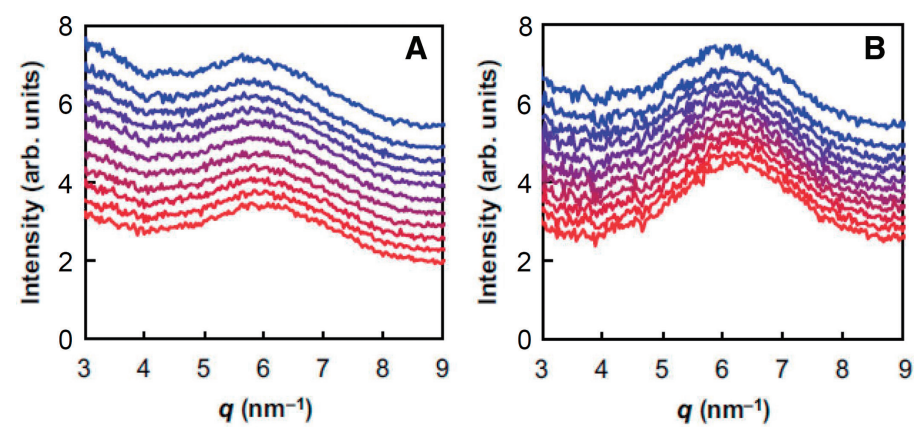


Fig. 7 Changes in X-ray diffraction intensity profiles for soft keratin filaments during the drying process in human stratum corneum: (A) SC treated with water and (B) SC treated with an aqueous solution of 10% glycerol. The blue to red curves shows continuous evolution from 0 to 20 min, with each curve plotted at 2 min intervals. The illustrated intensity profiles are shifted in the longitudinal direction.<sup>17)</sup>

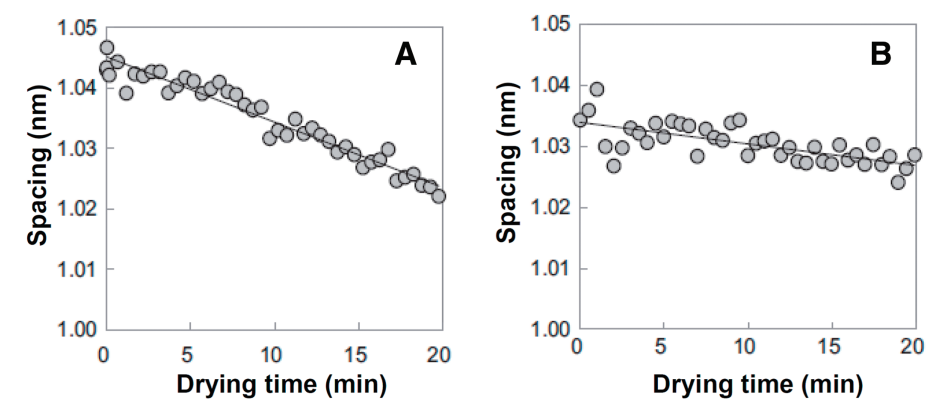


Fig. 8 Change in the spacing of the coiled-coil  $\alpha$ -helix chains of soft keratin over drying time: (A) human stratum corneum treated with water and (B) treated with an aqueous solution of 10% glycerol.<sup>17)</sup>

Table 1 Descendent slope of the spacing of the coiled-coil  $\alpha$ -helix chains of soft keratin over drying time during the drying process of human stratum corneum treated with water, and with aqueous solutions of 10% glycerol and 10% diglycerol. <sup>18)</sup>

Solution	Slope (mm/min)
Water	-0.0011
10% diglycerol	-0.0004
10% diglycerol	-0.0009

From this table, the difference between glycerol and diglycerol can be seen. This result indicates that glycerol (molecular weight [MW]: 92) can penetrate corneccytes and plays a role in retaining water for a long time, but diglycerol (MW: 166) does not penetrate corneccytes easily, as indicated by the lack of a significant difference in the slope between the diglycerol aqueous solution and water. As a result, glycerol interacts with the coiled-coil  $\alpha$ -helix chains of soft keratin to strengthen the binding of bound water in corneccytes, and on the other hand, molecules larger than glycerol, such as diglycerol, cannot cross the corneccyte envelope.

In the wide-angle region, Fig. 9A shows the XRD intensity profiles during the drying of hydrated human SC samples. At  $q \sim 15$  and  $17 \text{ nm}^{-1}$ , XRD peaks clearly appeared. These are the XRD peaks corresponding to the lattice spacings of ORTHO. In addition, during the drying of the hydrated SCsample, the decrease in the background gradient in the high-angle region is due to the reduction in water, with a broad XRD peak at  $q \sim 19 \text{ nm}^{-1}$ . Each peak at  $q \sim 15 \text{ or } 17 \text{ nm}^{-1}$  was analyzed by fitting to a Gaussian function with a straight background. The results of the spacing versus drying time are shown in Figs. 9B and 9C. As seen in these figures, the resolution in obtaining the spacing the change is extremely

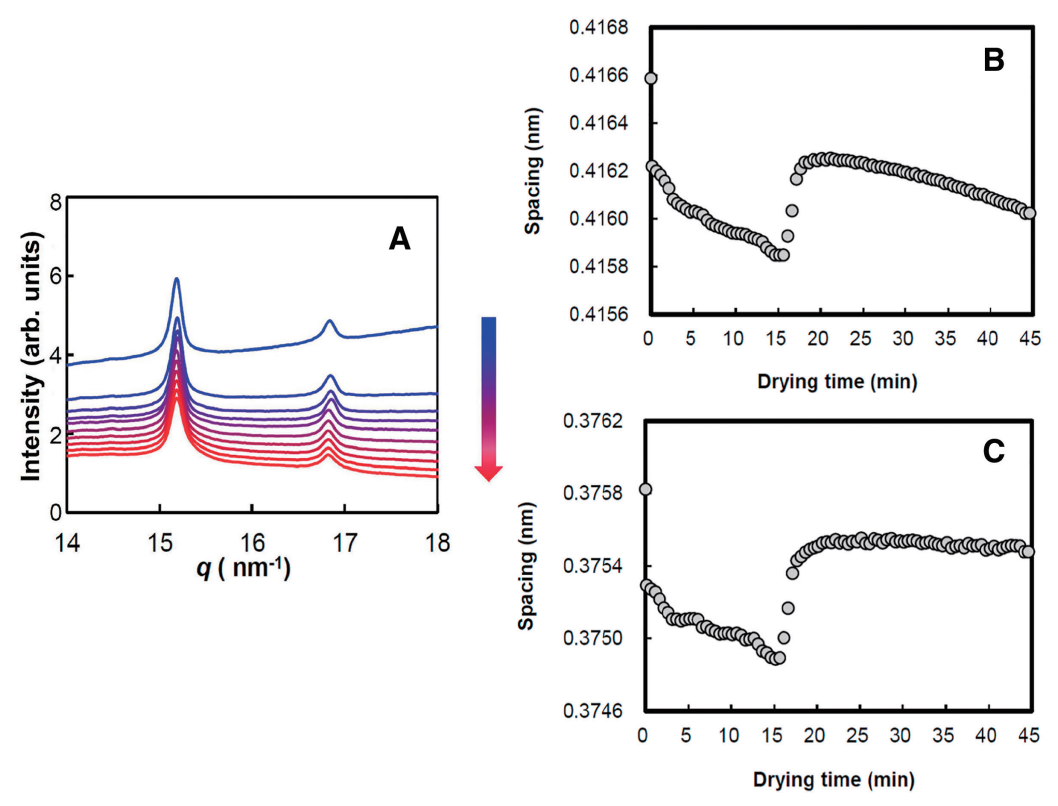


Fig. 9 (A) Change in X-ray diffraction intensity profiles of the orthorhombic hydrocarbon-chain packing structure during the drying process for stratum corneum treated with water. The blue to red curve shows the continuous evolution from 0 to 45 min, with each curve plotted at 5 min intervals for easy viewing. The illustrated intensity profiles are shifted in the longitudinal direction. (B, C) Change in the spacings of the orthorhombic hydrocarbon-chain packing structure of the hydrated human stratum corneum against drying time for spacings around 0.41 and around 0.37 nm, respectively.

high, and by using the solution cell, a change of approximately 0.00001 nm can be detected. However, with such high-resolution detection, it is impossible to avoid drift due to delicate changes in temperature, pressure, sample displacement, and so on. In fact, the plots in Figs. 9B and 9C show slight irregular changes, as can be seen from the behavior after 20 min. However, taking into consideration the results of other experiments comprehensively, this part might be almost flat. It is noted that the spacings in Figs. 9B and 9C vary systematically, and their coincidence is extremely high. Both spacings decrease rapidly immediately after drying, remain at a small value for a certain time thereafter, and finally increase to a large value and become almost constant. It was speculated that the second interval with a small value is a stable state having a water content of 25 wt%. <sup>17–19</sup> The interval during which the water content remains in the stable state is called the retention time. The order of retention time length was 10% diglycerol > 10% glycerol > water. It can be presumed that these retention times, prolonged by the polyols, are due to the interaction between the hydroxyl group of the polyols and the hydrophilic head group of the intercellular lipids. Recently, Toyoshima et al. <sup>19)</sup> showed that ORTHO and SLS are in the same domain. Therefore, the polyols penetrate the water layer of SLS and strengthen water regulation so as to maintain the water content at 25 wt%. As a result, glycerol increases the retention time, and diglycerol increases the retention time even further.

From the time-resolved XRD measurements, it was concluded that glycerol penetrates corneocytes and acts on soft keratin filaments, thereby forming bound water, while diglycerol penetrates the water layer in SLS, strongly enhancing the water regulation ability.

## 4.3. Disrupted SC and its repair

# 4.3.1. SC disrupted by sodium dodecyl sulfate

To study the effects of cosmetics on SC, it is necessary to narrow down what type of damaged skin is being targeted for repair. An anionic surfactant, sodium dodecyl sulfate (SDS), is widely used as an additive in commercial cleansing products. However, it has been pointed out that excessive treatment with SDS (MW: 288) results in an increase of TEWL in SC,<sup>37,38)</sup> and that SC lipids are extracted.<sup>39,40)</sup> Although these are the manifestations of cleansing-induced skin damage,

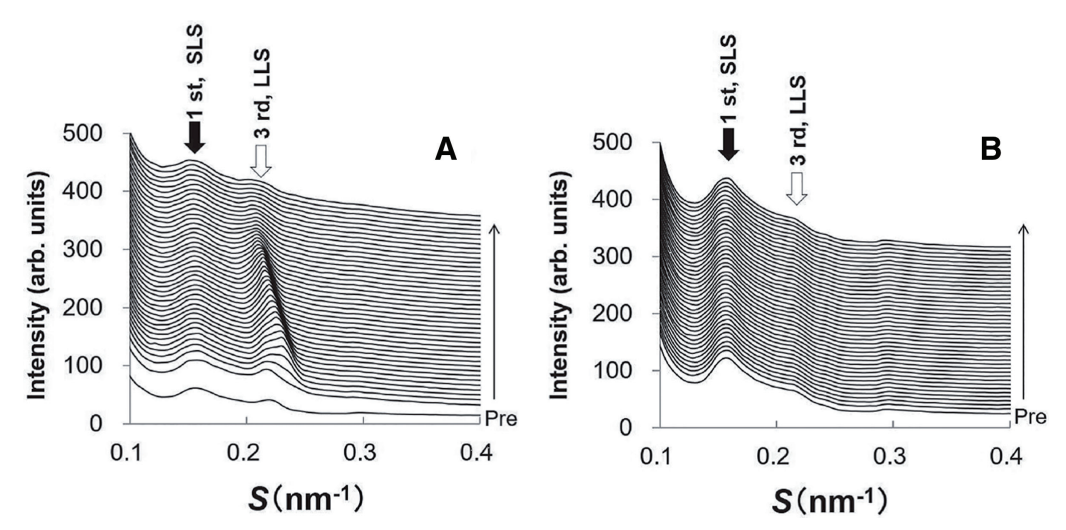


Fig. 10 Successive change in the small-angle X-ray diffraction profile of human stratum corneum samples treated with (A) an aqueous solution containing 10 wt% sodium dodecyl sulfate; (B) water alone. The profiles were recorded every 3 min for up to 129 min, where the profiles are successively shifted in the longitudinal direction; the thin arrow on the right indicates the direction of time. A white arrow indicates the third-order peak of the long-period lamellar structure (denoted as 3rd, LLS), and a filled arrow indicates the first-order peak of the short-period lamellar structure (denoted as 1st, SLS).<sup>41)</sup>

LLS, long-period lamellar structure; SLS, short-period lamellar structure

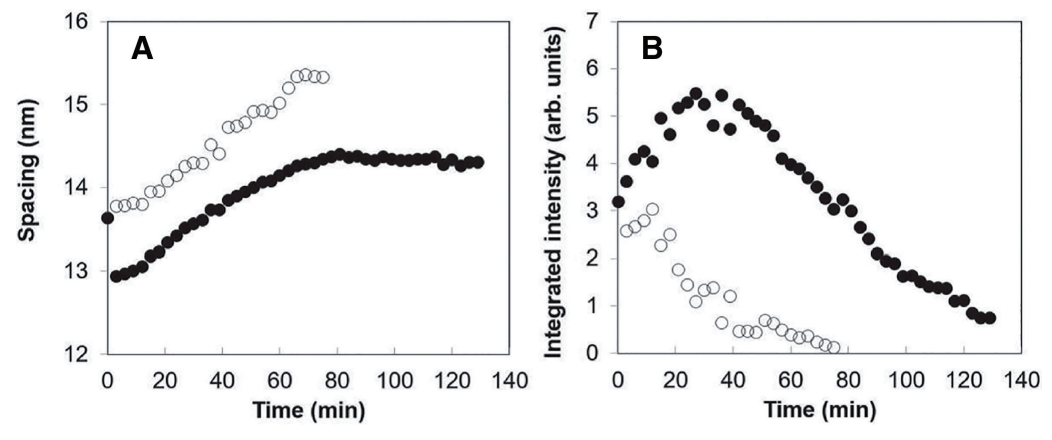


Fig. 11 (A) Changes in the spacing of the long-period lamellar structure when applying the 10 wt% sodium dodecyl sulfate solution to human stratum corneum. The initial spacing was about 13.7 nm. Immediately after applying the 10 wt% sodium dodecyl sulfate solution, the spacing was divided into 2, ○ and ●. One spacing (●) dropped rapidly and then increased. The other (○) increased monotonously. (B) Change in the integrated intensity. One of the intensities (●) increased, reached a maximum and then dropped; the other (○) decreased monotonously.<sup>41)</sup> arb. units, arbitrary units

it is necessary to clarify the underlying mechanism at the molecular level. For this purpose, when an SDS solution was applied to human SC, the XRD experiments were performed using the solution cell.<sup>41)</sup>

The solution cell was used to observe the structural changes when applying a solution containing 10 wt% SDS or water alone as a control to human SC at approximately 25°C. Human SC samples were exposed to a synchrotron X-ray beam for 30 s to obtain XRD profiles over small to wide angles. The small-angle XRD profiles for LLS and SLS of human SC after treatment with 10 wt% SDS and with water were observed as shown in Figs. 10A and 10B, respectively. A "Pre" profile is shown in Figs. 10A and 10B as a reference indicating the initial sample characteristics before the solution or water was applied. As seen in Figs. 10A, the third-order XRD peak of LLS appears clearly in human SC and is split into 2 peaks after application of SDS solution. Then, we analyzed the peak by fitting to 2 Gaussian functions and a straight line. The spacing indicated by a filled circle in Fig. 11A initially drops in a short time,

then gradually increases, and eventually saturates, while the spacing indicated by an open circle monotonically increases and becomes almost saturated. The integrated intensity was obtained from the analyzed results and is shown in Fig. 11B. The strong intensity indicated by the filled circle increases first, reaches a maximum, and eventually disappears, while the weak intensity indicated by the open circle monotonically decreases and eventually disappears. Thus, the above behavior indicates that SDS affected LLS via 2 routes. In the case of 1 wt% SDS treatment, <sup>41,42)</sup> the structural change exhibited similar behavior to that of 10 wt% SDS treatment, but because of the weak effect, the behavior on the filled circles in Figs. 11A and 11B can be mainly detected, and furthermore the change occurs slowly; as a result, the minimum of the spacing denoted by the filled circle in Fig. 11A appears with a delay. Besides, as shown in Fig. 10A, in the human SC treated with the SDS solution, the first-order peak of SLS does not show a significant change. As shown in Fig. 10B, in human SC treated with water alone, LLS and SLS did not show any significant changes in the XRD profile. In the hydrocarbon chain packing structure, no significant changes were observed upon the application of water as well as the SDS solution.

Regarding the effect of SDS on LLS, it is of interest to consider it based on the results of neutron scattering experiments on an SC lipid model.<sup>43)</sup> The results indicate that water molecules are located in 2 crystallographic positions in LLS in the model. One is near the unit cell boundary of LLS, and the other is in the interior region of this unit cell. Then, in SDS-treated human SC samples, incorporation of SDS molecules at these 2 positions could result in the splitting of the spacing and the decay of the intensity, that is, the destruction of LLS.

For LLS, a mixture of cholesterol and ceramides isolated from human SC revealed that only small amounts of LLS were present if ceramide (EOS) was removed from the mixture, suggesting that ceramides (EOS) play an important role in the formation of LLS. 44–46) Meanwhile, a decrease in the content of acylceramides, including ceramides (EOS), in SC has been associated with severe pathological consequences and with various adverse physiological effects on skin barrier function. 53–55) Therefore, LLS-disrupted human SC treated with SDS solution is one of the suitable SCs for further studies on functional repair.

# 4.3.2. Recovery of damaged SC by application of acylceramides

According to the above results, topical application of acylceramide appears to be an attractive approach to recover the barrier function of the damaged skin. Nakaune-Iijima et al.<sup>56)</sup> demonstrated that the application of acylceramide to the damaged skin promotes the recovery of the LLS. In the study by Nakaune-Iijima et al.,<sup>56)</sup> *in vitro* 3D reconstructed human epidermis (RHE) was used. The SC derived from the RHE sample was treated with 1 wt% SDS aqueous solution for 15 min, and then the disrupted SC was prepared. To examine the recovery from the disrupted LLS, the dispersion including acylceramide was applied. To obtain the acylceramide-included dispersion, a mixture was first prepared by mixing acylceramide (ceramide (EOS) or (EOP)) with cholesterol and 1,3-butylene glycol. Second, an aqueous dispersion of lecithin was added to the mixture. Third, the overall material was sonicated and emulsified to prepare nanoparticles. By dynamic light scattering analysis, the average diameter of the nanoparticles formed in the dispersion was about 10 nm. The recovery of LLS was assessed using small-angle XRD and transmission electron microscopy (TEM) analysis. In the XRD experiments, in the untreated SC a first-order diffraction peak of LLS was observed. From the XRD experiments, it was found that LLS was disrupted by application of the SDS solution and recovered by the acylceramide treatment. The TEM images also showed specific repeating patterns of LLS structures, indicating that topical acylceramide application promotes recovery of LLS.

There are 2 possible processes by which acylceramides are incorporated into the disrupted LLS: one is through the penetration of the nanoparticle into the SC, and the other is through trapping and reorganization of the nanoparticle on the surface of the SC, followed by the penetration of acylceramide molecules into the SC. The former requires the nanoparticle, with a diameter of ~10 nm, to penetrate the intercellular lipid matrix. Electron microscopy observation of fixed neonatal mouse skin showed that the width of the intercellular lipid spacing between adjacent corneocytes is 60–100 nm.<sup>57)</sup> Thus, the nanoparticle may be able to enter the intercellular lipid matrix. In this case, the nanoparticle should be observed within the SC. Meanwhile, the latter requires the reorganization of the nanoparticle on the SC surface, and therefore this organized structure must be observed. At present, it is not known which is the case.

# 4.4. Significance of disordered hydrocarbon-chain packing structure in skin function

4.4.1. Presence of disordered hydrocarbon-chain packing structure revealed by ethanol treatment and its penetration enhancement effect

When human SC was treated with ethanol, using the solution cell it was found, by chance, that the disordered hydrocarbon-chain packing structure dissolved in ethanol, whereas the ordered hydrocarbon-chain packing structure, ORTHO, was not affected significantly.<sup>58,59)</sup>

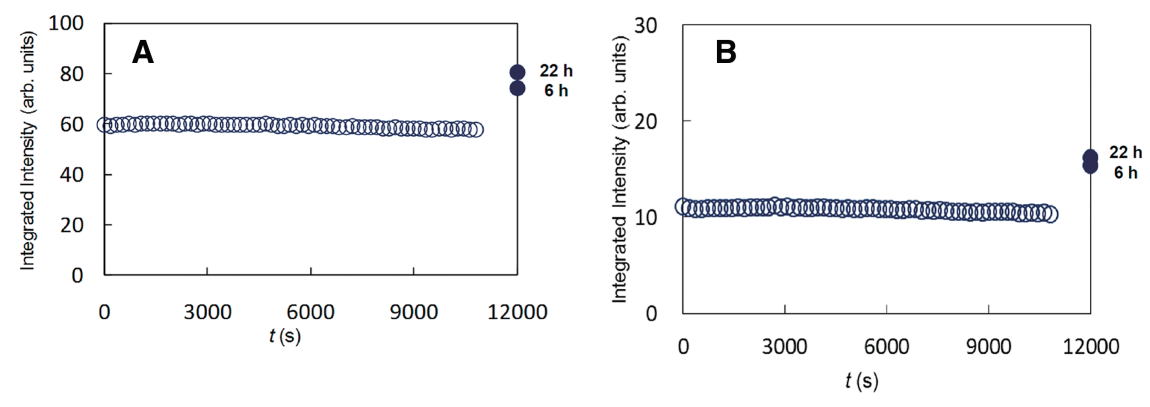


Fig. 12 (A) Time course of the X-ray diffraction integrated intensity for the spacings of about 0.41 nm and (B) about 0.37 nm. From 0 to 10200 s, a human stratum corneum sample was exposed to ethanol, then ethanol was removed from the stratum corneum, where for convenience, the data after removing ethanol for 6 and 22 h are shown at the position of 12000 s on the axis. arb. units, arbitrary units

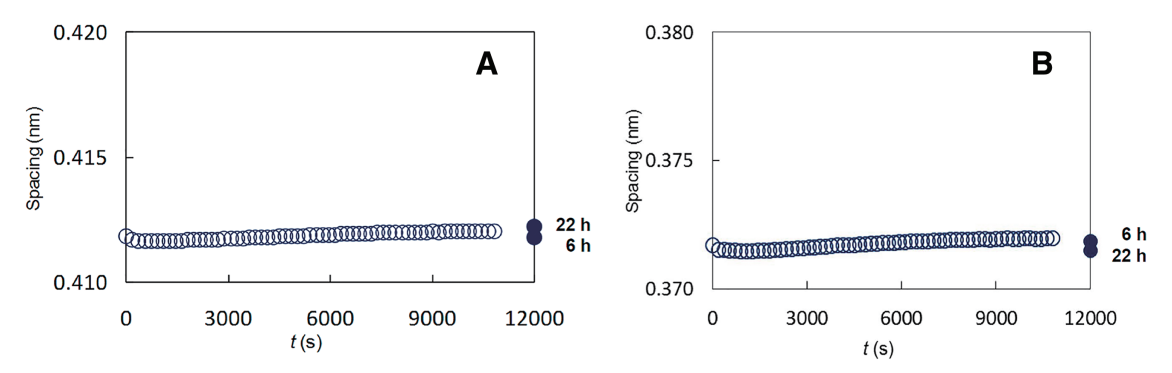


Fig. 13 (A) Time course of the spacings of about 0.41 nm and (B) about 0.37 nm obtained by X-ray diffraction. From 0 to 10200 s, a human stratum corneum sample was exposed to ethanol, then ethanol was removed from the stratum corneum, where, for convenience, the data after removing ethanol for 6 and 22 h are shown at the position of 12000 s on the axis.

In the experiments, human SC was immersed in ethanol from 0 to 10200 s. After that, ethanol was removed from the SC for up to 22 h. During this procedure, wide-angle XRD experiments were carried out. As shown in Figs. 12A and 12B, for the interval from 0 to 10200 s, the integrated intensity of the XRD peaks for ORTHO with the spacing 0.41 nm and 0.37 nm almost unchanged, respectively, but as ethanol was removed from the ethanol-treated SC, the integrated intensity increased and 22 h later became 1.4 times bigger for the spacing 0.41 nm and 1.5 times bigger for the spacing 0.37 nm in Figs. 12A and 12B, respectively. In some samples, the increase reached 2 times at the maximum. On the other hand, as shown in Figs. 13A and 13B, the spacings of 0.41 and 0.37 nm hardly changed not only during immersion in ethanol but also after removing the ethanol, respectively.

These results are summarized as follows:

- (a) Ethanol does not affect ORTHO and also is hard to extract the intercellular lipids in ORTHO.
- (b) When ethanol was removed from the ethanol-treated SC, the same structure as ORTHO before ethanol removal was formed.
- (c) Ethanol dissolved the disordered hydrocarbon-chain packing structure, the FLUID, resulting in a mixture of ethanol and the intercellular lipids.
  - (d) FLUID occupies a significant portion of the intercellular lipid matrix, which reaches 50%.

Ethanol is generally believed to be a chemical capable of enhancing drug penetration across the skin, but its mechanism is not fully understood. Bommannan et al.<sup>60)</sup> studied the action of ethanol on human SC using attenuated total reflectance infrared spectroscopy and found that no lipid extraction occurred and also no evidence for the induction of lipid disordering. Krill et al.<sup>61)</sup> studied the effect of ethanol on hairless mouse SC using Fourier transform infrared spectroscopy

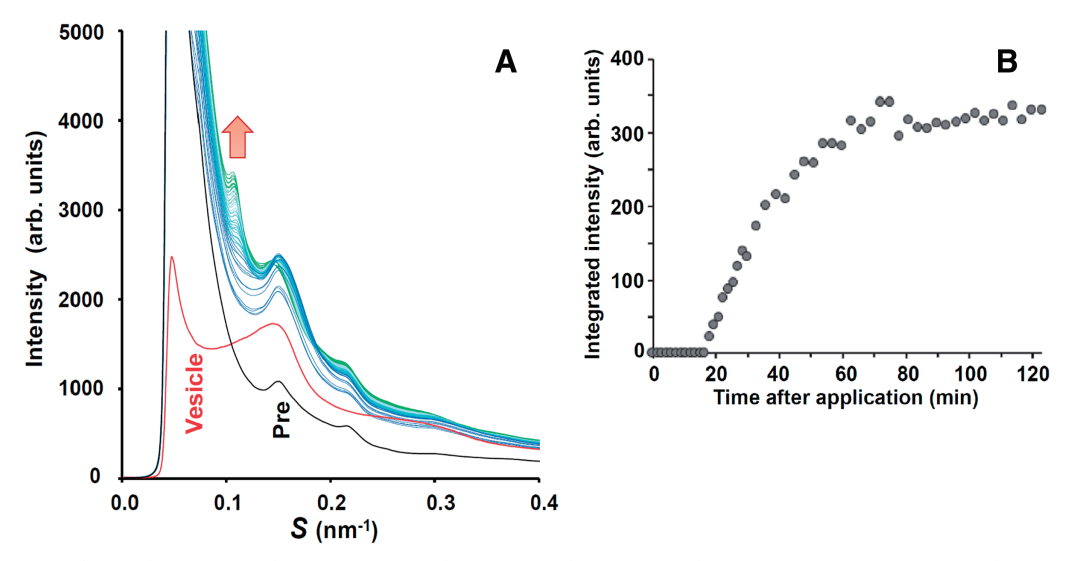


Fig. 14 (A) Time-dependent X-ray diffraction profile after application of the aqueous suspension of the nanoparticles to the stratum corneum: evolution of the profiles from dark blue to green curve (red arrow). Also shown are static X-ray diffraction profiles of the nanoparticle vesicles (red curve) and hairless mouse stratum corneum (black curve) before application of the aqueous suspension of the nanoparticles. (B) Change in the integrated intensity of the newly formed lamellar structure after application of the nanoparticle suspension to the stratum corneum. arb. units, arbitrary units

and found that ethanol does not affect the phase transition of ORTHO. These results are consistent with the present result (a). Based on the results (c) and (d), we propose one possible mechanism for the penetration enhancement mechanism of ethanol, that is, the lipids in FLUID were dissolved in ethanol, and FLUID with ethanol yields a much more fluidized mixture, and therefore not only hydrophobic but also hydrophilic drugs can more easily penetrate in the mixture.

Related to the above fact, it is interesting that alcohol-based disinfectants were widely used during the coronavirus disease 2019 pandemic without any reports of serious side effects.

# 4.4.2. Proportion of FLUID and 500 Da rule

As pointed out in the previous subsection 4.4.1, result (d) revealed that FLUID predominates in the intercellular lipid matrix and serves as the dominant permeation pathway for hydrophobic cosmetic and drug molecules. The existence of FLUID has been known for a long time, but the proportion of FLUID was first estimated by Doucet et al. in the following way<sup>4</sup>): The wide-angle XRD profile attributed only to intercellular lipids was obtained by subtracting the profile of a human SC sample delipidated with chloroform/methanol solvent from the profile before delipidation; by excluding the contribution of the profile due to soft keratin, we can obtain the wide-angle XRD profile only for the lipids in SC. Then, the proportion of FLUID was estimated to be about 80%. In this analysis, it was assumed that the lipids in FLUID and the ordered state (ORTHO and HEX) are extracted uniformly by chloroform/methanol treatment, but the lipids in FLUID might be extracted more vigorously than those in the ordered state. Therefore, it is very likely that the proportion of the lipids in FLUID is overestimated, that is, the proportion of the lipids in FLUID may be less than 80%.

On the other hand, the proportion of FLUID described in result (d) in subsection 4.4.1 may be underestimated because FLUID contains a large amount of cholesterol molecules that inhibit the formation of ORTHO and HEX, and also, probably, the formation of ORTHO or HEX requires sufficient time and appropriate growth conditions.

As a result, we currently propose that the proportion of FLUID is between 50% and 80% of the total intercellular lipids. Therefore, when considering the penetration of cosmetics or drugs, we should first take into account the pathway via FLUID. To investigate the properties of the FLUID region through which molecules penetrate, we estimated the average MW of the intercellular lipids in FLUID  $^{58,59}$ ) by tentatively calculating the sum of the population-weighted central MW based on data from van Smeden et al.<sup>1)</sup> As a result, the average MW is  $514 \pm 25$  Da. However, since cholesterol molecules (MW: 387) are excluded from the ordered hydrocarbon-chain packing structures (ORTHO and HEX), the average MW of the lipids in FLUID may be much smaller. Based on this result, when a hydrophobic molecule less than 500 Da is applied to SC, it is speculated that it merges with the lipids in FLUID and can diffuse and penetrate the FLUID region. A smaller lipophilic molecule diffuses more easily; on the contrary, a bigger molecule becomes difficult to diffuse since

the diffusion constant becomes smaller roughly in inverse proportion to the molecular size. However, we cannot exclude the penetration of nanoparticles and nanotubes with diameters smaller than the 60–100 nm width of the intercellular lipid region in the FLUID region, although they would require longer diffusion times.

Not only hydrophobic small molecules but also hydrophilic small molecules such as water molecules and molecules of natural moisturizing factors can penetrate SC. Such hydrophilic small molecules also permeate corneccytes and the narrow water layer of SLS, but can also permeate the tortuous pathways in FLUID.<sup>62)</sup> As mentioned above, solutions such as ethanol dissolve the molecules in FLUID and may enhance the penetration of larger substances such as ethosomes.<sup>63)</sup>

The high density of cholesterol molecules in FLUID may be involved in the penetration-enhancing effect. When corticosteroids are applied topically, it is likely that their penetration is enhanced due to the favorable correlation between the corticosteroids and cholesterol. In addition, the high density of cholesterol molecules appears to lead to the formation of cholesterol crystals.

# 4.5. Nanoparticles as a drug vehicle

## 4.5.1. Penetration of vitamin C and E derivatives loaded into phospholipid nanoparticles

Lipid nanoparticles have attracted attention from the viewpoint of cosmetic and pharmaceutical applications to the skin.<sup>64)</sup> Using liposomes to deliver cosmetics and drugs to and through human skin is controversial, as their function varies with type and composition.<sup>65)</sup> Here, we present one example,<sup>66)</sup> in which a nanoparticle consists of a phospholipid vesicle loaded with vitamin C and E derivatives (3-O-cetyl ascorbic acid [MW: 401] and tocopherol acetate [MW: 473], respectively), which are topical antioxidants.<sup>67)</sup> The nanoparticle vesicle formulations were prepared by mixing the vitamin C and E derivatives, soya phosphatidylcholine, and sodium cholate. Glycerol was also added to improve skin accumulation of the vitamin C and E derivatives in SC. In the vesicle, these small hydrophobic molecules, the vitamin C and E derivatives, can be entrapped; glycerol molecules can be trapped on the fully hydrated SC surface; and an edge activator, sodium cholate, is added to promote deformation of lipid bilayers.<sup>64)</sup> The vesicle size of the nanoparticle was approximately 120 nm.

Static small-angle XRD measurements were performed on an aqueous suspension of the nanoparticles of phospholipid vesicles loaded with vitamin C and E derivatives, as well as on hairless mouse SC, before the time-resolved measurements. The SC was hydrated to a water content of 80 wt%. As shown in Fig. 14, the static XRD profile for the vesicle is drawn with a red curve denoted as "Vesicle," and that for the SC is drawn with a black curve denoted as "Pre." In the profile for the suspension, broad peaks at about 0.14 and 0.28 nm<sup>-1</sup> (corresponding spacing: 7.1 nm) appear, which are the first- and second-order XRD peaks of the oligolamellar structure of the vesicle, respectively. In the profile for the SC, a broad first-order diffraction peak, clear second- to third-order diffraction peaks, and a broad fourth-order peak of LLS appear. After applying the aqueous suspension of the nanoparticles to the SC using the solution cell, time-resolved small-angle XRD measurements were performed. The SC sample was exposed to a synchrotron X-ray beam for 30 s, and the XRD profiles were recorded every 3 min up to 120 min.

After applying the aqueous suspension of the nanoparticles to the SC, as shown in Fig. 14A, a peak at  $S = 0.11 \text{ nm}^{-1}$ (corresponding spacing: 9.1 nm) related to the multilamellar structure newly appears and grows, probably on the flat surface of the SC. Since this peak lies between the first- and second-order peaks of LLS, the profile can be analyzed without any complicated operations by fitting it to a Gaussian function and a baseline given by Eq. (4). From the result of the analysis, the time course of integrated intensity was calculated as shown in Fig. 14B, where the evolution proceeded in 2 steps: (A) the integrated intensity is absent until about 16.5 min after application of the nanoparticle suspension, and (B) after this period, the integrated intensity gradually increases until 70 min and finally saturates. On the other hand, after 16.5 min, the peak intensity at S = 0.16 nm<sup>-1</sup> decreases inversely. However, it is not easy to analyze the behavior of this peak because at least 3 peaks contribute near  $S = 0.16 \text{ nm}^{-1}$ : the second-order diffraction peak of LLS, the first-order diffraction peak of SLS, and a peak due to the free nanoparticle vesicles (see the peak of vesicle in Fig. 14A). One possibility is that LLS is destroyed by the uptake of vitamin derivatives. Another possibility is that the number of free nanoparticle vesicles is reduced by forming the new lamellar structure on the surface of the SC. The spacing of the new lamellar structure, 9.1 nm, is larger than that of the nanoparticle vesicle, 7.1 nm. This could be a result of glycerol molecules localizing close to the head groups of the phospholipids and generating a water layer, and also might be due to transformation to a drug-free lamellar structure. For the penetration of the vitamin derivatives, it has been detected by other experiments that when the nanoparticle vesicle is applied to the SC, the vitamin derivatives can be released into the SC.<sup>66</sup>)

From the above results, it was proposed that (1) initially, the nanoparticle components accumulated around the SC surface; (2) the vitamin derivatives were released into the SC; and (3) simultaneously, the new drug-free lamellar structure grew on the SC surface. These events are supported by the phenomenon that a certain period is required to construct the

new lamellar structure, as shown in Fig. 14B. This proposal is consistent with the mechanism of "vesicle adsorption to and/or fusion with the stratum corneum (SC)" described in the paper by El Maghraby et al.<sup>65)</sup>

4.5.2. Nanoparticle composed of inverted hexagonal structure of lipids

In the case where a nanoparticle, formed by a 1-glyceryl monooleyl ether-based inverted hexagonal liquid-crystalline structure that captures flurbiprofen (MW: 244), and is applied to hairless mouse SC, similar behavior to that in subsection 4.5.1 was observed by time-resolved XRD using the solution cell.<sup>68)</sup> Prior to this measurement, static X-ray scattering experiments were performed on a flurbiprofen-loaded nanoparticle and a flurbiprofen-free nanoparticle, where in these nanoparticles the lattice constant of the (10) diffraction peak in the inverted hexagonal liquid-crystalline structure was observed at 5.9 and 6.1 nm, respectively.<sup>69)</sup> These XRD peaks appeared between the second- and third-order LLS peaks. When the nanoparticles with about 150 nm diameter were applied to the SC, the evolution proceeded in 3 steps: (A) in the first step, the (10) peak intensity of the hexagonal structure was absent until about 12 min; (B) in the second step, the (10) peak with the lattice constant of 6.1 nm for the flurbiprofen-free nanoparticle grew; (C) in the third step, in addition to this peak, the (10) peak with the lattice constant of 5.9 nm for the flurbiprofen-loaded nanoparticle appeared after about 40 min. From these results, it was speculated that the following events happen: In the first step, the interaction of the nanoparticles with the SC surface leads to a transient state before forming the drug-free inverted hexagonal structure, which is quite similar to what was observed in subsection 4.5.1. In the second step, the drug is released into SC in response to the formation of drug-free structures. In the third step, the drug-loaded structure appears by stacking on top of the drug-free structure. This may be because strain between the drug-free and drug-containing structures is relaxed as the distance from the SC surface increases, resulting in the drug-loaded structure stacking on the drug-free structure. As a result, when nanoparticles are applied to the SC, attention should be paid to events occurring on the SC surface.

# Conflict of Interest: None.

**Abbreviations:** DSC, differential scanning calorimetry; FLUID, fluid state; HEX, hexagonal hydrocarbonchain packing structure; LLS, long-period lamellar structure; MW, molecular weight; ORTHO, orthogonal hydrocarbon-chain packing structure; RHE, reconstructed human epidermis; SC, stratum corneum; SDS, sodium dodecyl sulfate; SLS, short-period lamellar structure; TEM, transmission electron microscopy; TEWL, transepidermal water loss; XRD, X-ray diffraction

#### References

- 1) J. van Smeden, W.A. Boiten, T. Hankemeier, R. Rissmann, J. A. Bouwstra, R. J. Vreeken, Biochim. Biophys. Acta Mol. Cell Biol. Lipids, 1841, 70–79 (2014)
- 2) J.A. Bouwstra, G.S. Gooris, J.A. van der Spek, W. Bras, J. Invest. Dermatol., 97, 1005–1012 (1991)
- 3) J.A. Bouwstra, G.S. Gooris, M.A. Salomons-de Vries, J.A. van der Spek, W. Bras, Int. J. Pharm., 84, 205–216 (1992)
- 4) J. Doucet, A. Potter, G. Baltenneck, Y.A. Domanov, J. Lipid Res., 55, 2380–2388 (2014)
- 5) I. Hatta, Dermato, 2, 79–108 (2022)
- 6) N. Ohta, S. Ban, H. Tanaka, S. Nakata, I. Hatta, Chem. Phys. Lipids, 123, 1-8 (2003)
- 7) D. Groen, G. S. Gooris, J. A. Bouwstra, Biophys. J., 97, 2242–2249 (2009)
- 8) H. Nakazawa, N. Ohta, I. Hatta, Chem. Phys. Lipids, 165, 238–243 (2012)
- 9) G.Ch. Charalambopoulou, Th.A. Steriotis, Th. Hauss, A.K. Stubos, N.K. Kanellopoulos, Physica B, 350, e603–e606 (2004)
- 10) D.C. Swartzendruber, P.W. Wertz, D.J. Kitko, K. C. Madison, D.T. Downing, J. Invest. Dermatol., 92, 251–257 (1989)
- 11) J.R. Hill, P. W. Wertz, Biochim. Biophys. Acta Biomembr., 1616, 121–126 (2003)
- 12) A. Narangifard, C.L. Wennberg, L. den Hollander, I. Iwai, H.M. Han, M. Lundborg, S. Masich, E. Lindahl, B. Daneholt, L. Norlén, J. Invest. Dermatol., 141, 1243–1253 (2021)
- 13) S.H. White, D. Mirejovsky, G.I. King, Biochemistry, 27, 3725–3732 (1988)
- 14) G.S.K. Pilgram, D.C.J. Vissers, H. van der Meulen, S. Pavel, S.P.M. Lavrijsen, J.A. Bouwstra, H.K. Koerten, J. Invest. Dermatol., 117, 710–717 (2001)
- 15) H. Nakazawa, T. Imai, I. Hatta, S. Sakai, S. Inoue, S. Kato, Biochim. Biophys. Acta Biomembr., 1828, 1424–1431 (2013)

- 16) I. Hatta, N. Ohta, K. Inoue, N. Yagi, Biochim. Biophys. Acta, 1758, 1830–1836 (2006)
- 17) T. Yamada, A. Habuka, I. Hatta, Int. J. Cosmet. Sci., 43, 38–47 (2021)
- 18) A. Habuka, T. Yamada, I. Hatta, SPring-8/SACLA Research Frontiers 2021, 104–105 (2022)
- 19) R. Toyoshima, K. Murashima, I. Hatta, Int. J. Cosmet. Sci., 47, 864–876 (2025)
- 20) G.Ch. Charalambopoulou, P. Karamertzanis, E.S. Kikkinides, A.K. Stubos, N.K. Kanellopoulos, A.Th. Papaioannou, Pharm. Res., 17, 1085–1091 (2000)
- 21) F. Briki, B. Busson, J. Doucet, Biochim. Biophys. Acta Protein Struct. Mol. Enzymol., 1429, 57–68 (1998)
- 22) N. Yagi, K. Aoyama, N. Ohta, PLoS One, 15, e0233131 (2020)
- 23) D. Horita, I. Hatta, M. Yoshimoto, Y. Kitao, H. Todo, K. Sugibayashi, Biochim. Biophys. Acta Biomembr., 1848, 1196–1202 (2015)
- 24) M. Green, A.M. Feschuk, N. Kashetsky, H.I. Maibach, Exp. Dermatol., 31, 1618–1631 (2022)
- 25) H. Tagami, Br. J. Dermatol., 171 (Suppl. 3), 29–33 (2014)
- 26) K. Walkley, J. Invest. Dermatol., 59, 225–227 (1972)
- 27) G. Imokawa, H. Kuno, M. Kawai, J. Invest. Dermatol., 96, 845–851 (1991)
- 28) P.J. Caspers, G.W. Lucassen, R. Wolthuis, H.A. Bruining, G.J. Puppels, Biospectroscopy, 4 (Suppl), S31–S39 (1998)
- 29) A. Sieg, J. Crowther, P. Blenkiron, C. Marcott, P.J. Matts. Proc. SPIE Int. Soc. Opt. Eng., 60930N, 60930N (2006)
- 30) M. Egawa, Analyst, 146, 1142–1150 (2021)
- 31) J.A. Bouwstra, A. de Graaff, G.S. Gooris, J. Nijsse, J.W. Wiechers, A.C. van Aelst, J. Invest. Dermatol., 120, 750–758 (2003)
- 32) M. Egawa, T. Hirao, M. Takahashi, Acta Derm. Venereol., 87, 4–8 (2007)
- 33) M. Egawa, T. Kajikawa, Skin Res. Technol., 15, 242–249 (2009)
- 34) M. Lodén, H. Olsson, T. Axéll, Y. Werner Linde, Br. J. Dermatol., 126, 137–141 (1992)
- 35) M. Egawa, M. Oguri, T. Kuwahara, M. Takahashi, Skin Res. Technol., 8, 212–218 (2002)
- 36) I. Hatta, H. Nakazawa, Y. Obata, N. Ohta, K. Inoue, N. Yagi, Chem. Phys. Lipids, 163, 381–389 (2010)
- 37) M. Denda, J. Koyama, R. Namba, I. Horii, Arch. Dermatol. Res., 286, 41–46 (1994)
- 38) S.M. Patil, P. Singh, H.I. Maibach, Int. J. Pharm., 110, 147–154 (1994)
- 39) G. Imokawa, S. Akasaki, Y. Minematsu, M. Kawai, Arch. Dermatol. Res., 281, 45–51 (1989)
- 40) C.L. Froebe, F.A. Simion, L.D. Rhein, R.H. Cagan, A. Kligman, Dermatology, 181, 277–283 (1990)
- 41) K. Yanase, I. Hatta, Int. J. Cosmet. Sci., 40, 44–49 (2018)
- 42) K. Yanase, I. Hatta, SPring-8/SACLA Research Frontiers 2017, 90–91 (2018)
- 43) E.H. Mojumdar, G.S. Gooris, D. Groen, D.J. Barlow, M.J. Lawrence, B. Demé, J.A. Bouwstra, Biochim. Biophys. Acta Biomembr., 1858, 1926–1934 (2016)
- 44) T.J. McIntosh, M. Stewart, D.T. Downing, Biochemistry, 35, 3649–3653 (1996)
- 45) J.A. Bouwstra, G.S. Gooris, F.E.R. Dubbelaar, A.M. Weerheim, A.P. IJzerman, M. Ponec, J. Lipid Res., 39, 186–196 (1998)
- 46) J.A. Bouwstra, F.E.R. Dubbelaar, G.S. Gooris, A.M. Weerheim, M. Ponec, Biochim. Biophys. Acta Biomembr., 1419, 127–136 (1999)
- 47) S. Motta, M. Monti, S. Sesana, R. Caputo, S. Carelli, R. Ghidoni, Biochim. Biophys. Acta Mol. Basis Dis., 1182, 147–151 (1993)
- 48) A.P. Lavrijsen, J.A. Bouwstra, G.S. Gooris, A. Weerheim, H.E. Boddé, M. Ponec, J. Invest. Dermatol., 105, 619–624 (1995)
- 49) D.G. Paige, N. Morse-Fisher, J.I. Harper, Br. J. Dermatol., 131, 23–27 (1994)
- 50) S. Motta, M. Monti, S. Sesana, L. Mellesi, R. Ghidoni, R. Caputo, Arch. Dermatol., 130, 452–456 (1994)
- 51) H. Farwanah, K. Raith, R.H. Neubert, J. Wohlrab, Arch. Dermatol. Res., 296, 514–521 (2005)
- 52) J. van Smeden, M. Janssens, W.A. Boiten, V. van Drongelen, L. Furio, R.J. Vreeken, A. Hovnanian, J.A. Bouwstra, J. Invest. Dermatol., 134, 1238–1245 (2014)
- 53) G. Imokawa, A. Abe, K. Jin, Y. Higaki, M. Kawashima, A. Hidano, J. Invest. Dermatol., 96, 523–526 (1991)
- 54) J. Rogers, C. Harding, A. Mayo, J. Banks, A. Rawlings, Arch. Dermatol. Res., 288, 765–770 (1996)
- 55) J. Ishikawa, Y. Shimotoyodome, S. Ito, Y. Miyauchi, T. Fujimura, T. Kitahara, T. Hase, Arch. Dermatol. Res., 305, 151–162 (2013)

- 56) A. Nakaune-Iijima, A. Sugishima, G. Omura, H. Kitaoka, T. Tashiro, S. Kageyama, I. Hatta, Chem. Phys. Lipids, 215, 56–62 (2018)
- 57) P.M. Elias, D.S. Friend, J. Cell Biol., 65, 180–191 (1975)
- 58) I. Hatta, N. Ohta, H. Nakazawa, Pharmaceutics, 9, 1–9 (2017)
- 59) I. Hatta, H. Nakazawa, N. Ohta, T. Uchino, K. Yanase, J. Oleo Sci., 70, 1181–1199 (2021)
- 60) D. Bommannan, R.O. Potts, R.H. Guy, J. Control. Release, 16, 299–304 (1991)
- 61) S.L. Krill, K. Knutson, W.I. Higuchi, Biochim. Biophys. Acta Biomembr., 1112, 273–280 (1992)
- 62) J.A. Bouwstra, M. Ponec, Biochim. Biophys. Acta Biomembr., 1758, 2080–2095 (2006)
- 63) E. Touitou, N. Dayan, L. Bergelson, B. Godin, M. Eliaz, J. Control. Release, 65, 403-418 (2000)
- 64) P.L. Honeywell-Nguyen, J.A. Bouwstra, Drug Discov. Today. Technol., 2, 67–74 (2005)
- 65) G.M.M.El Maghraby, A.C. Williams, B.W. Barry, J. Pharm. Pharmacol., 58, 415–429 (2006)
- 66) T. Fushimi, T. Uchino, Y. Miyazaki, I. Hatta, M. Asano, H. Fujino, R. Suzuki, S. Fujimori, D. Kamiya, Y. Kagawa, Int. J. Pharm., 548, 192–205 (2018)
- 67) J. Aguilera, M.V. de Gálvez, C. Sánchez, E. Herrera-Ceballos, J. Dermatol. Sci., 66, 216–220 (2012)
- 68) T. Uchino, S. Kato, I. Hatta, Y. Miyazaki, T. Suzuki, K. Sasaki, Y. Kagawa, Int. J. Pharm., 555, 259–269 (2019)
- 69) T. Uchino, A. Murata, Y. Miyazaki, T. Oka, Y. Kagawa, Chem. Pharm. Bull., 63, 334–340 (2015)